Variable Action Period Predictive Flux Control Strategy for Permanent Magnet Synchronous Machines

Zhanfeng Song, *Senior Member, IEEE*, Siyu Hu, and Zhongqiang Bao

***Abstract*—This article introduces a method to achieve the variable action period (VAP) of voltage vector in the finite control set model predictive control (FCS-MPC). In the conventional FCS-MPC, the control behavior is limited since the action period of a voltage vector is normally fixed to the sampling period. This article aims to enhance the control performances by means of regulating the action period of selected voltage vectors, together with the selection of an optimal control action. A VAP-based predictive flux control strategy is thus proposed. The optimal voltage vector and its optimal action period are both obtained by means of a two-step cost function minimization. In this manner, the future states of the control objectives are taken into account in the construction of cost function. The action period for the selected voltage vectors is no longer fixed to the sampling period, which provides an additional control freedom to obtain improved reference tracking behaviors. Experimental validations and comparison studies demonstrate that enhanced steady-state performances as well as excellent dynamic behaviors can both be obtained with the proposed strategy adopted.**

***Index Terms*—Flux control, permanent magnet synchronous machines (PMSMs), predictive control, variable action period (VAP).**

I. INTRODUCTION

PERMANENT magnet synchronous machines (PMSMs) have been broadly used in various industrial applications including high-precision servo-control systems, electric vehicles, and wind power generation systems, due to its advantages such as high power density, high efficiency, and wide operating range [1]–[4]. Therefore, the control strategy of PMSM has always been a research focus in this field.

The conventional field-oriented control (FOC) [5] and direct torque control (DTC) [6], [7] are usually applied in the three-phase electrical drive control systems. Generally, in the conventional FOC strategy, the independent control of electromagnetic torque and rotor flux can be achieved by using the rotating coordinate transformation [8]. Typically, the linear controller (e.g., proportional integral controller) is adopted to regulate the control objectives and, then, it generates the continuous voltage reference. Note that the continuous voltage reference applied to the motor should be synthesized by a modulator such as space vector pulse-width modulation (PWM) module [9]. However, the motor drives are highly nonlinear systems, which complicate the obtention of an approximated linearized transfer function for the controller design. In addition, the implementation of the proportional integral (PI) controller in the present-day digital platforms demands discretization of the controller. Differently, the control of torque and flux is achieved by applying the hysteresis bound and lookup table in the DTC [10], [11]. Since the absence of modulator, a faster transient response can be expected with DTC adopted, while it always has higher current harmonic components and torque ripples.

Apart from the mainstream vector control strategies, the model predictive control (MPC), especially its finite control set (FCS) version, is regarded as a promising candidate in the control of electrical drives. Over the past few years, a considerable amount of research work has been conducted to demonstrate the superiorities of this control strategy [12], [13]. With FCS-MPC adopted, a cost function is first constructed and it flexibly incorporates the control objectives, which typically correspond to torque and flux, respectively [14]. This cost function is, then, minimized with the discrete switching nature and finite control actions of power converters taken into account. By evaluating the effects of all candidate voltage vectors, the switching state corresponding to the minimum cost function is selected as the optimal voltage vector and is finally applied [14]–[18]. When compared with the DTC, MPC is a more flexible control scheme since the multivariable case can be considered and the resulting controller is easy to implement [19], [20]. Besides, due to the inherent characteristics of behavior prediction and direct manipulation of converter switching states, predictive control strategies have many advantages when compared with traditionally linear-controller-based FOC, including highly dynamic behaviors, easy inclusion of nonlinearities, and satisfied capability to achieve the multiple-input multiple-output control [21]–[25].

However, one typical challenge for FCS-MPC lies in its steady-state performances. The reference signal cannot be accurately tracked. The reason is that the converter control is

---

Manuscript received May 11, 2019; revised September 22, 2019; accepted November 11, 2019. Date of publication November 17, 2019; date of current version February 20, 2020. This work was supported by the National Natural Science Foundation of China under Grants 51877150 and 51477113. Recommended for publication by Associate Editor H. Hofmann. *(Corresponding author: Zhanfeng Song.)*

Z. Song and S. Hu are with Tianjin University, School of Electrical and Information Engineering, Tianjin 300072, China (e-mail: zfsong@tju.edu.cn; syhu@tju.edu.cn).

Z. Bao is with Guangxi Power Grid Co., Ltd, Guangxi 530023, China (e-mail: bao_zq@qq.com).

Color versions of one or more of the figures in this article are available online at http://ieeexplore.ieee.org.

Digital Object Identifier 10.1109/TPEL.2019.2953941

typically achieved by modifying the product of voltage vector and its application period. When the FCS-MPC is applied, the selected voltage vector will be held for the whole sampling period, i.e., its application period is fixed. The only control freedom is the selection of different voltage vectors. Owing to the limited number of possible switching states, the control objective cannot be accurately achieved [26], [27]. Even though the steady-state performances can be improved by increasing the switching frequency and decreasing the application period of selected voltage vectors, it consequently generates higher switching losses [28].

One straightforward method to solve this problem is to expand the possible switching states, which provides regulation flexibility regarding the magnitude of candidate voltage vectors. However, this can only be realized by introducing multiple switching levels, which normally requires hardware adjustment. Differently, Arahal *et al.* [29] proposed a novel way to solve this problem. In this method, the application period of voltage vectors is adjusted in a discrete way. Each sampling period is divided into several subperiods. The cost function is, then, evaluated with all switching states and all these subperiods taken into account. A closer reference tracking and enhanced steady-state performances can then be obtained. However, as the optimization process is conducted over the product of all switching states and all subperiods, a very heavy computational burden can be expected [29]. Similarly, a variable switching frequency method is proposed in [30]. The variable switching frequency is achieved by developing the modulator in the FPGA, which is capable of changing the sampling time on each period. The maximum switching frequency of the inverter is fixed and the possible switching frequencies are predefined within a range from 1 kHz to the maximum value with 1 kHz increments. Then, the cost function minimization is achieved by the exhausted calculation of all possible switching frequencies. However, the steady-state performances can only be partially improved as the application period of voltage vectors cannot be arbitrarily adjusted.

Another approach to improve the control performances is to flexibly regulate the voltage vector's action period (i.e., the duration of voltage vector in every prediction step). The variable action period (VAP) can be achieved by changing the sampling period [31], [32]. In [32], the optimal switching state that can achieve the closest trajectory to the lead-pursuit direction is first selected. The action period of the optimal switching state is chosen to minimize the deviation of the reference trajectory from the end point after applying the optimal switching state [32]. Note that the optimal switching state is obtained based on the deviation of the control objective from its reference at the present moment. That means the selected optimal switching state, which does not take the future state into consideration, may be improper with the evolution of time.

The main contribution of this article is to enhance the control performances by means of regulating the action period of selected voltage vectors, together with the selection of an optimal control action. A VAP-based predictive flux control strategy is, thus, proposed. The optimal voltage vector and its optimal action period are both obtained by means of a two-step cost function minimization. In this manner, the future states of the control objectives are taken into account in the construction of cost function. The action period for the selected voltage vectors is no longer fixed to the sampling period, which provides an additional control freedom to obtain improved reference tracking behaviors.

The rest of this article is structured as follows. The mathematical model of the PMSM system is introduced in Section II. Section III presents an overview of the conventional FCS-MPC and the proposed VAP-based MPC strategy (VAP-MPC). The proposed method and its digital implementation are explained in detailed in Sections IV and V, respectively. In Section VI, the effectiveness of the proposed control strategy and its superiority over the conventional method are experimentally validated. Finally, the conclusion is given in Section VII.

II. PMSM MODEL

In the following, complex vectors will be adopted to represent electrical variables and expressed by using boldface letters. For example, the stator current can be expressed as $\boldsymbol{i}_\mathrm{s} = i_\alpha + \mathrm{j}i_\beta$, where i_α and i_β are α- and β-axes current components, respectively. The voltage equation of the surface-mounted PMSM in the stator coordinates is given as

$$\boldsymbol{u}_\mathrm{s}(t) - R_\mathrm{s}\boldsymbol{i}_\mathrm{s}(t) - \frac{\mathrm{d}\boldsymbol{\Psi}_\mathrm{s}(t)}{\mathrm{d}t} = 0 \tag{1}$$

where $\boldsymbol{u}_\mathrm{s}$, $\boldsymbol{i}_\mathrm{s}$, $\boldsymbol{\Psi}_\mathrm{s}$, and R_s represent the stator voltage vector, the stator current vector, the stator flux vector, and the stator resistance, respectively. The time dependence of vectors is given by t. Moreover, the stator flux vector $\boldsymbol{\Psi}_\mathrm{s}$ is expressed as

$$\boldsymbol{\Psi}_\mathrm{s}(t) = L_\mathrm{s}\boldsymbol{i}_\mathrm{s}(t) + \boldsymbol{\Psi}_\mathrm{r}(t) \tag{2}$$

where L_s stands for the stator inductance. $\boldsymbol{\Psi}_\mathrm{r}$ denotes the rotor flux vector in the stator coordinates, which is given by

$$\boldsymbol{\Psi}_\mathrm{r}(t) = \psi_\mathrm{r}\mathrm{e}^{\mathrm{j}\vartheta_\mathrm{e}(t)} \tag{3}$$

where ψ_r and ϑ_e represent the rotor flux amplitude and the electrical angle of rotor position, respectively. As the stator resistance is small and its influence on the stator windings could be consequently neglected, (1) could be rewritten as

$$\frac{\mathrm{d}\boldsymbol{\Psi}_\mathrm{s}(t)}{\mathrm{d}t} = \boldsymbol{u}_\mathrm{s}(t). \tag{4}$$

Furthermore, (4) could be expressed in the discrete-time domain as

$$\boldsymbol{\Psi}_\mathrm{s}(k+1) = \boldsymbol{\Psi}_\mathrm{s}(k) + T_\mathrm{s}\boldsymbol{u}_\mathrm{s}(k) \tag{5}$$

where T_s denotes the sampling period. It can be found from (5) that the desired stator flux vector at time instant $(k+1)T_\mathrm{s}$ could be achieved by modulating the stator voltage vector $\boldsymbol{u}_\mathrm{s}(k)$. Besides, the electromagnetic torque of PMSM can be expressed as

$$T_\mathrm{e} = \frac{1.5\,n_\mathrm{p}}{L_\mathrm{s}}|\boldsymbol{\Psi}_\mathrm{r} \times \boldsymbol{\Psi}_\mathrm{s}| = \frac{1.5\,n_\mathrm{p}}{L_\mathrm{s}}\psi_\mathrm{r}\psi_\mathrm{s}\sin(\vartheta_\mathrm{s} - \vartheta_\mathrm{e}) \tag{6}$$

where n_p is the number of pole pairs, ψ_s is the amplitude of stator flux, and ϑ_s is the angle of stator flux vector. Meanwhile,

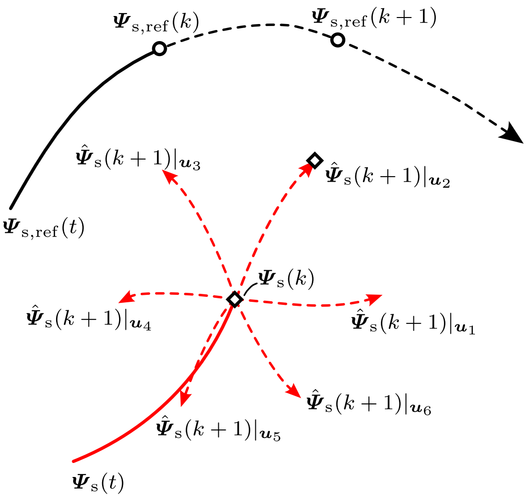

Fig. 1. Stator flux trajectory with FCS-MPC adopted when the voltage vectors take action between the time instants $kT_{\rm s}$ and $(k+1)T_{\rm s}$.

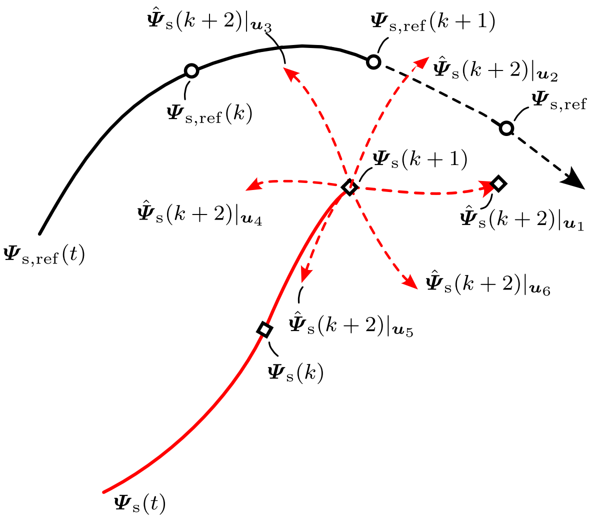

Fig. 2. Stator flux trajectory with FCS-MPC adopted when the voltage vectors take action between the time instants $(k+1)T_{\rm s}$ and $(k+2)T_{\rm s}$.

(6) can be rearranged as

$$\vartheta_{\rm s} - \vartheta_{\rm e} = \arcsin\left(\frac{L_{\rm s}T_{\rm e}}{1.5\, n_{\rm p}\psi_{\rm r}\psi_{\rm s}}\right). \tag{7}$$

It can be found from (7) that, assuming that the amplitudes of stator flux vector and rotor flux vector are constants, the desired torque can be obtained by regulating the angle $\vartheta_{\rm s}$.

III. OVERVIEW OF THE CONVENTIONAL FCS-MPC AND THE PROPOSED VAP-MPC

A. *Conventional FCS-MPC*

When the conventional FCS-MPC is adopted to achieve flux vector control for PMSMs, a cost function that reflects the control errors under different control actions is first constructed. Eight basic voltage vectors of a voltage source converter (VSC) are, then, evaluated based on this cost function. The voltage vector corresponding to the minimum cost function is, then, selected as the optimal one and finally applied. It should be noted that, with FCS-MPC adopted, the action period of selected voltage vector is fixed to the sampling period $T_{\rm s}$.

Fig. 1 demonstrates the stator flux trajectory with FCS-MPC adopted when the voltage vector takes action between the time instants $kT_{\rm s}$ and $(k+1)T_{\rm s}$. In this figure, $\boldsymbol{u}_1 \sim \boldsymbol{u}_6$ stand for the active voltage vectors of VSC. The subscript $_{\rm ref}$ and hat $^\wedge$ represent the reference and predicted flux vector, respectively. The red solid line and black solid line denote the trajectories of the stator flux vector and its reference, respectively. The red dotted lines that originate from the square point $\boldsymbol{\Psi}_{\rm s}(k)$ correspond to the possible evolution generated by separate action of active voltage vectors. Based on the variables sampled at time instant $kT_{\rm s}$, the predicted flux vectors at time instant $(k+1)T_{\rm s}$ are calculated for each possible control action. Obviously, for the example shown in Fig. 1, the voltage vector $\boldsymbol{u}_2$ is the optimal control action in accordance with the control objective. This optimal vector will be applied and held during the whole sampling period between time instants $kT_{\rm s}$ and $(k+1)T_{\rm s}$. This process will be repeated in the next execution of the control scheme, as shown in Fig. 2, in which $\boldsymbol{u}_1$ will be the optimal vector then. Note that the control objective (e.g., reference stator flux vector) cannot be accurately tracked due to the finite number of voltage vectors and their fixed application period. Therefore, a large flux vector error generally exists during operation, which causes torque ripples and current harmonics. A typical way to obtain improved steady-state performances is to adopt reduced application period $T_{\rm s}$. However, this will result in higher switching frequency and increasing switching losses.

B. *Proposed VAP-MPC*

Different from the conventional FCS-MPC, the proposed VAP-MPC aims to enhance the control performances by means of regulating the action period of selected voltage vectors. In other words, the action period for the selected voltage vector is no longer fixed to $T_{\rm s}$, which provides an additional control freedom to obtain the improved reference tracking behaviors.

As both the control states (i.e., stator flux vector and its reference signal) vary with time, the determination of the optimal voltage vector as well as its action period requires some anticipation. The future trajectory of the stator flux vector can be obtained based on the sampled signals at the current sampling instant and the prediction process. The trajectory of the reference flux vector is a circularity and its future state is characterized as a function of action period. Therefore, a cost function that reflects the deviation between the stator flux vector and its reference value can be constructed and represented as a function of action period. The optimal voltage vector and its optimal action period can, then, be obtained by means of a two-step cost function minimization.

The evolution of stator flux vector with the proposed VAP-MPC adopted is shown in Fig. 3. Obviously, the action periods of six basic voltages are different form each other. Meanwhile, when $\boldsymbol{u}_2$ is applied and held for a period of $t_{\rm i2}$, the minimum

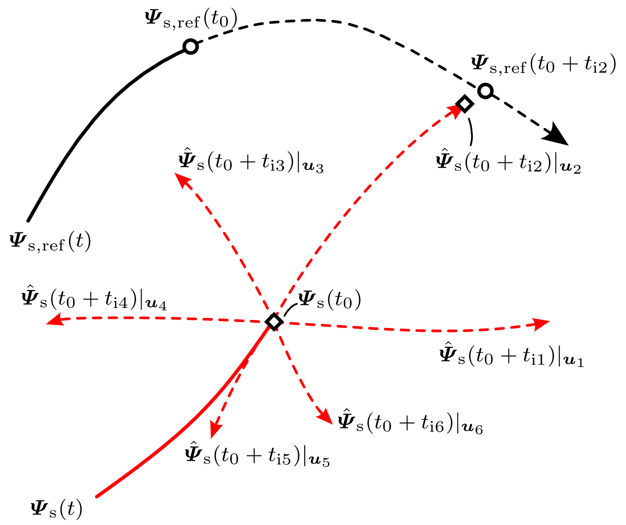

Fig. 3. Stator flux trajectory when the proposed VAP-MPC is adopted.

error between the reference and predicted flux vector can be obtained.

Different from the conventional FCS-MPC, the action period of voltage vector is not fixed in the proposed method. By adding a new degree of freedom about the action period t in the control algorithm, a more suitable voltage vector and corresponding action period can, thus, be obtained. Consequently, the stator flux linkage can track its reference value more accurately, and the torque ripples as well as the harmonic contents in three-phase currents can be effectively reduced.

IV. PREDICTIVE FLUX CONTROL BASED ON VAP

A. *Determination of Optimal Action Period for Each Voltage Vector*

In the proposed strategy, the optimal voltage vector and its optimal action period are obtained by means of a two-step cost function minimization. The first step is to calculate the optimal action periods of the voltage vectors. Note that the determination of the optimal voltage vector as well as its action period needs corresponding anticipation since the control objectives vary with time. As demonstrated in Fig. 4, t_0 stands for the current time instant. $\boldsymbol{\Psi}_{\rm s}(t_0)$ and $\boldsymbol{\Psi}_{\rm s,ref}(t_0)$ denote the actual and reference values of a stator flux vector at the current time instant t_0, respectively. Apparently, as is demonstrated in Fig. 4(a), the optimal voltage vector $\boldsymbol{u}_2$ is applied to reduce the control error $\Delta\boldsymbol{\Psi}_{\rm s}$ between the actual and reference stator flux vectors. The trajectory of actual flux vector is denoted by a red solid line, reference flux vector by a blue solid line, and flux vector error a by blue dotted line. Note that because the actual and reference flux vectors generally move in the different speed, their trajectories will not cross each other. That means the flux vector error cannot be reduced to zero but to a minimum value. This phenomenon is more clear in Fig. 4(b). As shown in the figure, with the evolution of time, the red solid line goes over the blue solid line without intersecting it. Besides, the magnitude of flux vector error (length of blue dotted line) also varies over time. More specifically, it first decreases with time before the minimum error is obtained, and then increases. Therefore, there exists a unique time instant t, at which the magnitude of flux vector error reaches its minimum value. The optimal action period for voltage vector $\boldsymbol{u}_{\rm i}$ is denoted by $t_{\rm i}$. At time instant $t_0+t_{\rm i}$, the predicted stator flux vector and reference stator flux vector can be expressed as

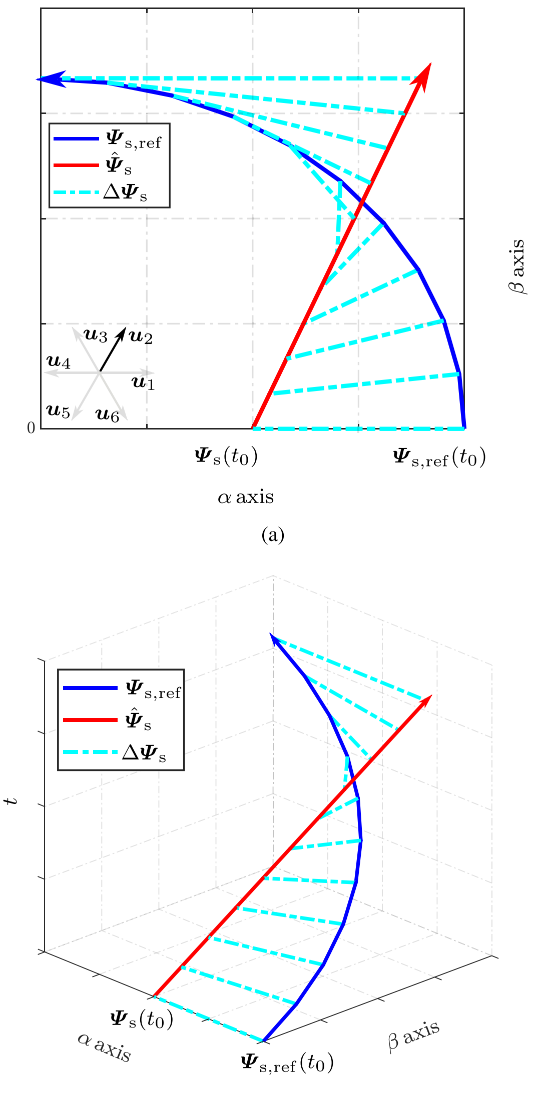

(a)

(b)

Fig. 4. Schematic diagram of stator flux trajectory. (a) Two-dimensional graph of stator flux trajectory. (b) Three-dimensional graph of stator flux trajectory.

$$\hat{\boldsymbol{\Psi}}_{\rm s}(t_0+t_{\rm i}) = \boldsymbol{\Psi}_{\rm s}(t_0) + \boldsymbol{u}_{\rm i}t_{\rm i} \tag{8}$$

$$\boldsymbol{\Psi}_{\rm s,ref}(t_0+t_{\rm i}) = \boldsymbol{\Psi}_{\rm s,ref}(t_0)\cdot {\rm e}^{{\rm j}\omega_{\rm e}t_{\rm i}}. \tag{9}$$

Therefore, at time instant $t_0+t_{\rm i}$, the flux vector error under the action of $\boldsymbol{u}_{\rm i}$ is given by

$$\begin{aligned}\Delta\boldsymbol{\Psi}_{\rm s}(t_{\rm i})|_{\boldsymbol{u}_{\rm i}} &= \boldsymbol{\Psi}_{\rm s,ref}(t_0+t_{\rm i}) - \hat{\boldsymbol{\Psi}}_{\rm s}(t_0+t_{\rm i})\\ &= \boldsymbol{\Psi}_{\rm s,ref}(t_0)\cdot {\rm e}^{{\rm j}\omega_{\rm e}t_{\rm i}} - \boldsymbol{\Psi}_{\rm s}(t_0) - \boldsymbol{u}_{\rm i}t_{\rm i}.\end{aligned} \tag{10}$$

It can be seen from (10) that the flux vector error is a function of action period t_{i}. A cost function representing the deviation between the reference stator flux vector and the predicted stator flux vector can be constructed as

$$g = \left[\Delta\boldsymbol{\Psi}_{\mathrm{s}}(t_{\mathrm{i}})|_{\boldsymbol{u}_{\mathrm{i}}}\right]^2. \tag{11}$$

As depicted in Fig. 4, when $\boldsymbol{u}_2$ is applied, the cost function g first decreases with time before the minimum error is obtained, and then increases. Therefore, the optimal action period t_{i} in accordance with the minimum cost function can be obtained by solving

$$\frac{\mathrm{d}g}{\mathrm{d}t_{\mathrm{i}}} = \frac{\mathrm{d}\left[\Delta\boldsymbol{\Psi}_{\mathrm{s}}(t_{\mathrm{i}})|_{\boldsymbol{u}_{\mathrm{i}}}\right]^2}{\mathrm{d}t_{\mathrm{i}}} = 0. \tag{12}$$

Thus, the optimal action period t_{i} for each voltage vector $\boldsymbol{u}_{\mathrm{i}}$ can be obtained, which corresponds to the minimum flux vector error. This calculation process will be conducted for all candidate voltage vectors. Note that the calculation of the optimal action period t_{i} is a time-consuming task and the corresponding simplification is needed. Therefore, in order to reduce the computational burden, the simplified selection process of candidate voltage vector is introduced in Section V.

B. *Selection of Optimal Voltage Vector*

After the optimal action period of each candidate voltage vector is calculated according to (12), the selection of optimal voltage vector from all candidate vectors (i.e., the second step of two-step cost function minimization) should, then, be conducted. The selection process is presented as follows. If the calculated t_{i} for one specific voltage vector is a negative value, it means that the corresponding voltage vector should act in the opposite direction. Under this situation, this voltage vector should be discarded. Subsequently, by substituting the remaining candidate voltage vectors and the corresponding action periods into the cost function g, the voltage vector corresponding to the minimum cost function is selected as the optimal one. The optimal voltage vector $\boldsymbol{u}_{\mathrm{opt}}$ can be described as

$$\boldsymbol{u}_{\mathrm{opt}} = \min_{\boldsymbol{u}_{\mathrm{i}}} g = \min_{\boldsymbol{u}_{\mathrm{i}}} \left[\Delta\boldsymbol{\Psi}_{\mathrm{s}}(t_{\mathrm{i}})|_{\boldsymbol{u}_{\mathrm{i}}}\right]^2. \tag{13}$$

V. DIGITAL IMPLEMENTATION

A. *VAP Versus Fixed Sampling Frequency*

In order to simplify the algorithm implementation, the sampling interval is set to a fixed value and the state of the switching devices is changed at most once within one sampling period. In order to describe the calculation process in more detail and without loss of generality, Fig. 5 is depicted as a typical example of the switching schematic diagram. The sampling instant is fixed and the sampling interval is T_{s}. Besides, in Fig. 5, it is assumed that the sequence of optimal voltage vectors is $\boldsymbol{u}_6(101)$, $\boldsymbol{u}_0(000)$, $\boldsymbol{u}_5(001)$, and $\boldsymbol{u}_4(011)$. The number in parentheses represents the working states of three-phase switching devices: 1 represents that the upper bridge arm works, while 0 implies that the lower bridge arm works. For clarity and better understanding, subscripts I and II are adopted to denote the sequence index of the optimal voltage vector. Taking time instant $(k-1)T_{\mathrm{s}}$ as an example, the first optimal voltage vector is $\boldsymbol{u}_{\mathrm{I}}(k-1)$ and the following are $\boldsymbol{u}_{\mathrm{II}}(k-1)$ and $\boldsymbol{u}_{\mathrm{III}}(k-1)$. Similarly, their corresponding action periods are $t_{\mathrm{I}}(k-1)$, $t_{\mathrm{II}}(k-1)$, and $t_{\mathrm{III}}(k-1)$, respectively.

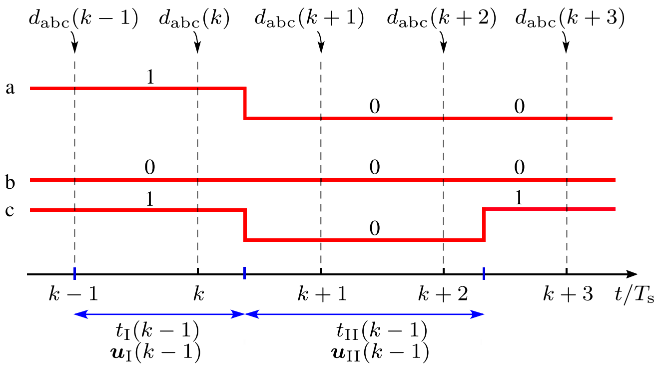

Fig. 5. Diagram of voltage vector switching when $T_{\mathrm{s}} \leq t_{\mathrm{I}}(k-1) < 2T_{\mathrm{s}}$.

Considering the time instant $(k-1)T_{\mathrm{s}}$, the voltage vector $\boldsymbol{u}_{\mathrm{I}}(k-1)(101)$ as well as its action period $t_{\mathrm{I}}(k-1)$, and the next optimal voltage vector $\boldsymbol{u}_{\mathrm{II}}(k-1)(000)$ as well as its action period $t_{\mathrm{II}}(k-1)$ are known variables, which are obtained in the previous sampling period. $d_{\mathrm{abc}}(k-1)$ is the three-phase duty cycle signals, which is calculated in the previous sampling interval and updated at time instant $(k-1)T_{\mathrm{s}}$. Specifically, for the case shown in Fig. 5, the duty cycles can be expressed as

$$d_{\mathrm{a}}(k-1) = d_{\mathrm{c}}(k-1) = 1, \quad d_{\mathrm{b}}(k-1) = 0. \tag{14}$$

Since the action period of selected voltage vectors is not fixed, the switching states may be changed within one sampling interval, as depicted in Fig. 5. Therefore, the way to update the duty cycle signals is an extremely important part of the proposed control algorithm and needs to be further discussed in detail.

B. *Update of Duty Cycle Signals*

The update of duty cycle signals includes different modes, which correspond to different voltage vector switching situations shown as follows.

1) $t_{\mathrm{I}}(k-1) \geq 2T_{\mathrm{s}}$: The schematic diagram of switching sequence under the situation of $t_{\mathrm{I}}(k-1) \geq 2T_{\mathrm{s}}$ is shown in Fig. 6.

Obviously, in this case, the voltage vector $\boldsymbol{u}_{\mathrm{I}}(k-1)$ will continue to act during the time period from kT_{s} to $(k+1)T_{\mathrm{s}}$ (i.e., k_{th} interval). Therefore, the duty cycle to be updated at time instant kT_{s} is the same as the previous one, resulting in

$$d_{\mathrm{abc}}(k) = d_{\mathrm{abc}}(k-1). \tag{15}$$

For the convenience of the following calculation, $\boldsymbol{u}_{\mathrm{I}}(k)$, $t_{\mathrm{I}}(k)$, $\boldsymbol{u}_{\mathrm{II}}(k)$, and $t_{\mathrm{II}}(k)$ need to be updated accordingly, which can be written as

$$\begin{cases} \boldsymbol{u}_{\mathrm{I}}(k) = \boldsymbol{u}_{\mathrm{I}}(k-1), t_{\mathrm{I}}(k) = t_{\mathrm{I}}(k-1) - T_{\mathrm{s}} \\ \boldsymbol{u}_{\mathrm{II}}(k) = \boldsymbol{u}_{\mathrm{II}}(k-1), t_{\mathrm{II}}(k) = t_{\mathrm{II}}(k-1). \end{cases} \tag{16}$$

2) $T_{\mathrm{s}} \leq t_{\mathrm{I}}(k-1) < 2T_{\mathrm{s}}$: The schematic diagram of switching sequence under the situation of $T_{\mathrm{s}} \leq t_{\mathrm{I}}(k-1) < 2T_{\mathrm{s}}$ is

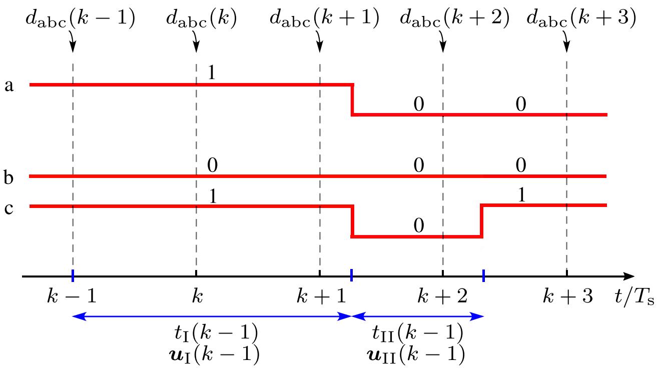

Fig. 6. Schematic diagram of voltage vector switching when $t_{\mathrm{I}}(k-1) \geq 2T_{\mathrm{s}}$.

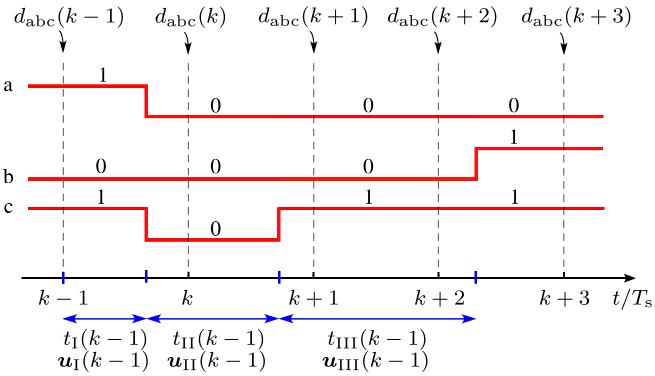

Fig. 7. Diagram of a voltage vector switching when $t_{\mathrm{I}}(k-1) < T_{\mathrm{s}}$ and $t_{\mathrm{I}}(k-1) + t_{\mathrm{II}}(k-1) < 2T_{\mathrm{s}}$.

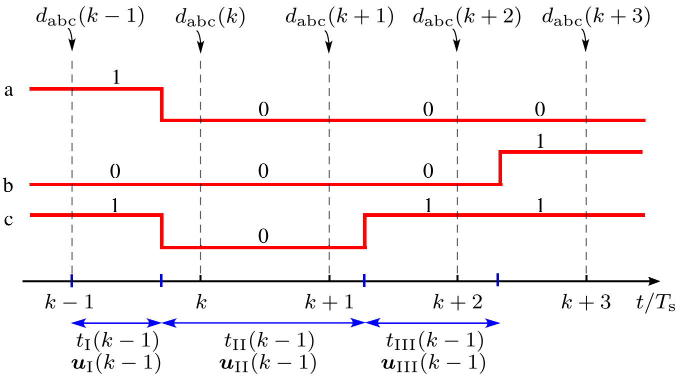

Fig. 8. Diagram of a voltage vector switching when $t_{\mathrm{I}}(k-1) < T_{\mathrm{s}}$ and $t_{\mathrm{I}}(k-1) + t_{\mathrm{II}}(k-1) \geq 2T_{\mathrm{s}}$.

depicted in Fig. 5. As shown in the figure, the voltage vector $\boldsymbol{u}_{\mathrm{I}}(k-1)$ takes action between time instants $(k-1)T_{\mathrm{s}}$ and kT_{s}, and, then, the voltage vector will switch from $\boldsymbol{u}_{\mathrm{I}}(k-1)$ to $\boldsymbol{u}_{\mathrm{II}}(k-1)$ between time instants kT_{s} and $(k+1)T_{\mathrm{s}}$. The duty cycle $d_{\mathrm{abc}}(k)$ is, then, updated as

$$d_{\mathrm{a}}(k) = d_{\mathrm{c}}(k) = \frac{t_{\mathrm{I}}(k-1) - T_{\mathrm{s}}}{T_{\mathrm{s}}}, \quad d_{\mathrm{b}}(k) = 0. \tag{17}$$

Furthermore, $\boldsymbol{u}_{\mathrm{I}}(k)$, $t_{\mathrm{I}}(k)$, $\boldsymbol{u}_{\mathrm{II}}(k)$, and $t_{\mathrm{II}}(k)$ need to be updated, which is the same as (16).

3) $t_{\mathrm{I}}(k-1) < T_{\mathrm{s}}$: When $t_{\mathrm{I}}(k-1) < T_{\mathrm{s}}$, the voltage vector $\boldsymbol{u}_{\mathrm{I}}(k-1)$ will end its action before the time instant kT_{s} and, then, switch to $\boldsymbol{u}_{\mathrm{II}}(k-1)$. The duty cycle signals to be updated at kT_{s} are, then, determined based on $t_{\mathrm{I}}(k-1)$ and $t_{\mathrm{II}}(k-1)$. The subsequent calculation process includes two cases explained as follows.

1) $t_{\mathrm{I}}(k-1) + t_{\mathrm{II}}(k-1) < 2T_{\mathrm{s}}$. In this situation, the switching diagram is shown in Fig. 7. $\boldsymbol{u}_{\mathrm{II}}(k-1)$ will end its action between time instants kT_{s} and $(k+1)T_{\mathrm{s}}$. A new optimal voltage vector needs to be applied subsequently. It is worth noting that, in order to calculate the duty cycles, the following optimal voltage vector $\boldsymbol{u}_{\mathrm{III}}(k-1)$, which takes action sequentially after the action of $\boldsymbol{u}_{\mathrm{II}}(k-1)$, should be obtained before the time instant kT_{s}. The determination of $\boldsymbol{u}_{\mathrm{III}}(k-1)$ and $t_{\mathrm{III}}(k-1)$ is conducted based on the two-step cost function minimization process mentioned in Section IV and the corresponding t_0 is equal to $kT_{\mathrm{s}} + t_{\mathrm{I}}(k-1) + t_{\mathrm{II}}(k-1)$.
The duty cycle to be updated at time instant kT_{s} could be determined according to $t_{\mathrm{I}}(k-1)$, $t_{\mathrm{II}}(k-1)$, $\boldsymbol{u}_{\mathrm{II}}(k-1)$, and $\boldsymbol{u}_{\mathrm{III}}(k-1)$, resulting in

$$\begin{aligned} d_{\mathrm{a}}(k) &= d_{\mathrm{b}}(k) = 0, \\ d_{\mathrm{c}}(k) &= \frac{2T_{\mathrm{s}} - t_{\mathrm{I}}(k-1) - t_{\mathrm{II}}(k-1)}{T_{\mathrm{s}}}. \end{aligned} \tag{18}$$

Then, $\boldsymbol{u}_{\mathrm{I}}(k)$, $t_{\mathrm{I}}(k)$, $\boldsymbol{u}_{\mathrm{II}}(k)$, and $t_{\mathrm{II}}(k)$ need to be updated as

$$\begin{cases} \boldsymbol{u}_{\mathrm{I}}(k) = \boldsymbol{u}_{\mathrm{II}}(k-1), \\ t_{\mathrm{I}}(k) = t_{\mathrm{II}}(k-1) + t_{\mathrm{I}}(k-1) - T_{\mathrm{s}} \\ \boldsymbol{u}_{\mathrm{II}}(k) = \boldsymbol{u}_{\mathrm{III}}(k-1), t_{\mathrm{II}}(k) = t_{\mathrm{III}}(k-1). \end{cases} \tag{19}$$

2) $t_{\mathrm{I}}(k-1) + t_{\mathrm{II}}(k-1) \geq 2T_{\mathrm{s}}$. The corresponding switching diagram is shown in Fig. 8. This situation is quite similar to the case when $t_{\mathrm{I}}(k-1) + t_{\mathrm{II}}(k-1) < 2T_{\mathrm{s}}$, except that $\boldsymbol{u}_{\mathrm{II}}(k-1)$ acts for a whole period between the time instant kT_{s} and $(k+1)T_{\mathrm{s}}$.

Therefore, the duty cycle $d_{\mathrm{abc}}(k)$ could be directly obtained according to $\boldsymbol{u}_{\mathrm{II}}(k-1)$. For the case shown in Fig. 8, the duty cycle is calculated as

$$d_{\mathrm{a}}(k) = d_{\mathrm{b}}(k) = d_{\mathrm{c}}(k) = 0. \tag{20}$$

$\boldsymbol{u}_{\mathrm{I}}(k)$, $t_{\mathrm{I}}(k)$, $\boldsymbol{u}_{\mathrm{II}}(k)$, and $t_{\mathrm{II}}(k)$ could, then, be similarly updated by using (19).

C. Pursue Problem and Delay Compensation

As well as the actual value of the stator flux vector, its reference signal also varies with time. The trajectory of reference flux vector is a circularity and its future state can be represented as a function of action period. This pursue problem should be taken into account in the control process. Besides, in a practical digital implementation process, due to the finite computation time, the optimal voltage vector obtained in the current interval can only take action at next period, which naturally introduces a one-sampling-period time delay. This delay needs to be taken into account when the optimal voltage vector together with its application time is determined.

The case shown in Fig. 7 is taken as an example here. When $t_{\mathrm{I}}(k-1) < T_{\mathrm{s}}$, the optimal action vector $\boldsymbol{u}_{\mathrm{III}}(k-1)$ and its action time $t_{\mathrm{III}}(k-1)$ need to be calculated. The calculation process with both the pursue problem and one-sampling-period time delay taken into consideration can be explained as follows. At the time instant $(k-1)T_{\mathrm{s}}$, the stator current $\boldsymbol{i}_{\mathrm{s}}(k-1)$ and the rotor electrical angular position $\vartheta_{\mathrm{e}}(k-1)$ can be obtained by the sampling schemes. According to (2) and (3), the stator and rotor flux vectors at time instant $(k-1)T_{\mathrm{s}}$ are obtained as

$$\begin{cases} \boldsymbol{\Psi}_{\mathrm{s}}(k-1) = L_{\mathrm{s}}\boldsymbol{i}_{\mathrm{s}}(k-1) + \boldsymbol{\Psi}_{\mathrm{r}}(k-1) \\ \boldsymbol{\Psi}_{\mathrm{r}}(k-1) = \psi_{\mathrm{r}}\mathrm{e}^{\mathrm{j}\vartheta_{\mathrm{e}}(k-1)}. \end{cases} \tag{21}$$

For convenience, t_{p} is introduced here and is expressed as

$$t_{\mathrm{p}} = (k-1)T_{\mathrm{s}} + t_{\mathrm{I}}(k-1) + t_{\mathrm{II}}(k-1) + t_{\mathrm{III}}(k-1). \tag{22}$$

According to (5), the predicted stator flux vector at time instant t_{p} could be written as

$$\begin{aligned} \hat{\boldsymbol{\Psi}}_{\mathrm{s}}(t_{\mathrm{p}}) = {} & \boldsymbol{\Psi}_{\mathrm{s}}(k-1) + \boldsymbol{u}_{\mathrm{I}}(k-1)t_{\mathrm{I}}(k-1) \\ & + \boldsymbol{u}_{\mathrm{II}}(k-1)t_{\mathrm{II}}(k-1) + \boldsymbol{u}_{\mathrm{III}}(k-1)t_{\mathrm{III}}(k-1). \end{aligned} \tag{23}$$

The corresponding reference stator flux vector at the same instant is

$$\boldsymbol{\Psi}_{\mathrm{s,ref}}(t_{\mathrm{p}}) = \psi_{\mathrm{s,ref}}\mathrm{e}^{\mathrm{j}\vartheta_{\mathrm{s,ref}}(k-1)+\mathrm{j}\omega_{\mathrm{e}}[t_{\mathrm{I}}(k-1)+t_{\mathrm{II}}(k-1)+t_{\mathrm{III}}(k-1)]} \tag{24}$$

where $\psi_{\mathrm{s,ref}}$ represents the magnitude of the stator flux and $\vartheta_{\mathrm{s,ref}}$ denotes the angle of the reference stator flux vector. According to (7), this angle is given by

$$\vartheta_{\mathrm{s,ref}}(k-1) = \vartheta_{\mathrm{e}}(k-1) + \arcsin\left(\frac{L_{\mathrm{s}}T_{\mathrm{e,ref}}}{1.5\,n_{\mathrm{p}}\psi_{\mathrm{r}}\psi_{\mathrm{s,ref}}}\right) \tag{25}$$

where $T_{\mathrm{e,ref}}$ represents the torque reference.

The control error between the reference stator flux vector and its predicted value at time instant t_{p} is

$$\Delta\boldsymbol{\Psi}_{\mathrm{s}}(t_{\mathrm{p}})|_{\boldsymbol{u}_{\mathrm{III}}} = \boldsymbol{\Psi}_{\mathrm{s,ref}}(t_{\mathrm{p}}) - \hat{\boldsymbol{\Psi}}_{\mathrm{s}}(t_{\mathrm{p}}). \tag{26}$$

With respect to each candidate voltage vector for the selection of $\boldsymbol{u}_{\mathrm{III}}(k-1)$, $t_{\mathrm{III}}(k-1)$ can be obtained by substituting (26) into (12) and solving the equation. Eight different action periods corresponding to eight basic voltage vectors are obtained. Specifically, the negative action periods and the corresponding candidate voltage vectors should be discarded.

Subsequently, by substituting the candidate voltage vectors and their action period into (13), the optimal voltage vector $\boldsymbol{u}_{\mathrm{III}}(k-1)$ and its action period $t_{\mathrm{III}}(k-1)$ can be determined based on cost function minimization.

D. Simplified Selection Process Based on Adjacent Voltage Vectors

In order to reduce the computational burden and average switching frequency, a simplified selection process based on adjacent voltage vectors is adopted in this article. The simplified candidate voltage vector group in every prediction step is updated based on the previous optimal voltage vector and a predefined lookup table, as shown in Table I. More specifically, when the previous optimal vector is a nonzero voltage vector, the candidate vector group contain itself, its adjacent two active voltage vectors, and a zero voltage vector (either $\boldsymbol{u}_0$ or $\boldsymbol{u}_7$ will be determined with the aim of reducing switching). When the previous optimal voltage vector is a zero voltage vector, the next optimal one will be selected in eight basic voltage vectors. After the candidate voltage vector group is determined, the cost function will be evaluated for each of the voltage vectors in this group. The flowchart of the proposed VAP-MPC is demonstrated in Fig. 9.

TABLE I
CANDIDATE VOLTAGE VECTOR GROUP AND THE PREVIOUS OPTIMAL VECTOR

Previous optimal vector $\boldsymbol{u}$	Candidate voltage vector group $\boldsymbol{U}_{\mathrm{c}}$
$\boldsymbol{u}_0$	$[\boldsymbol{u}_0\sim\boldsymbol{u}_7]$
$\boldsymbol{u}_1$	$[\boldsymbol{u}_0,\boldsymbol{u}_1,\boldsymbol{u}_2,\boldsymbol{u}_6]$
$\boldsymbol{u}_2$	$[\boldsymbol{u}_1,\boldsymbol{u}_2,\boldsymbol{u}_3,\boldsymbol{u}_7]$
$\boldsymbol{u}_3$	$[\boldsymbol{u}_0,\boldsymbol{u}_2,\boldsymbol{u}_3,\boldsymbol{u}_4]$
$\boldsymbol{u}_4$	$[\boldsymbol{u}_3,\boldsymbol{u}_4,\boldsymbol{u}_5,\boldsymbol{u}_7]$
$\boldsymbol{u}_5$	$[\boldsymbol{u}_0,\boldsymbol{u}_4,\boldsymbol{u}_5,\boldsymbol{u}_6]$
$\boldsymbol{u}_6$	$[\boldsymbol{u}_1,\boldsymbol{u}_5,\boldsymbol{u}_6,\boldsymbol{u}_7]$
$\boldsymbol{u}_7$	$[\boldsymbol{u}_0\sim\boldsymbol{u}_7]$

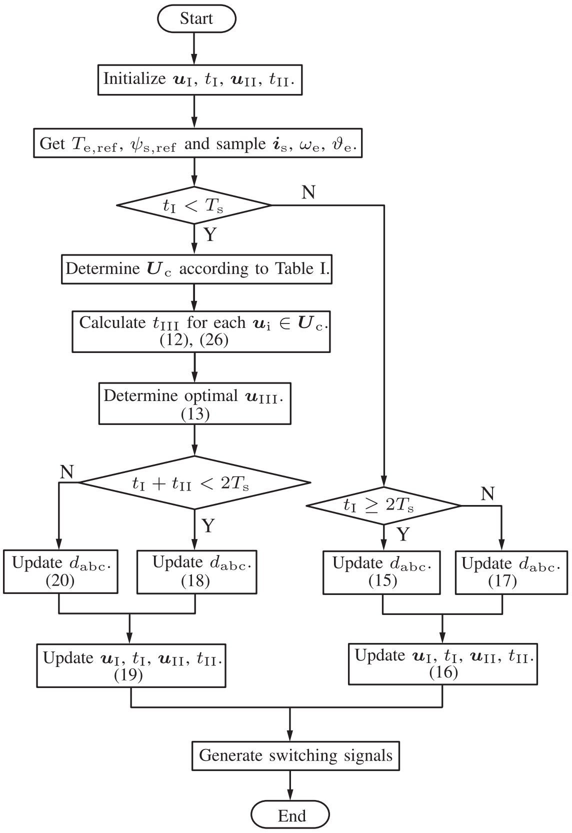

Fig. 9. Flowchart of the proposed VAP-MPC method.

VI. EXPERIMENTAL VALIDATION

The proposed method is implemented on a 2.3-kW surface-mounted PMSM, which is coaxially connected with a 3-kW load machine. The load machine is controlled by Siemens PM250. The control algorithms for PMSM are implemented based on a

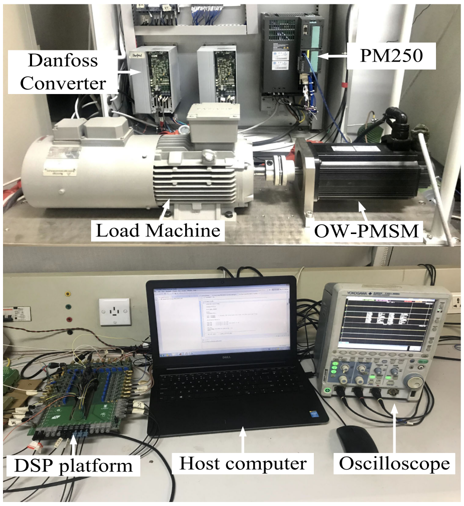

Fig. 10. Picture of the test rig.

TABLE II
SYSTEM PARAMETERS

Parameter	Symbol	Value
PMSM parameters:		
Rated power	P_{N}	2.3 kW
Rated speed	ω_{N}	1500 r/min
Rated torque	T_{N}	15 N·m
Rated stator current	i_{N}	7 A
Number of pole pairs	n_{p}	2
Stator resistance	R_{s}	2.25 Ω
Stator inductance	L_{s}	18.75 mH
Rotor flux amplitude	ψ_{r}	0.79 Wb
Load machine parameters:		
Rated power	P_{N}	3 kW
Rated speed	ω_{N}	1435 r/min
Rated torque	T_{N}	20 N·m
Rated stator current	i_{N}	6.7 A

TMS320F28379D digital signal processor. The test rig diagram is shown in Fig. 10. Detailed parameters of the surface-mounted PMSM and the load machine are shown in Table II.

A. VAP Method Verification

Fig. 11 shows the three-phase PWM waveforms when the conventional FCS-MPC and the proposed VAP-MPC are applied, respectively. In the experiment, the torque reference is set to 10 N·m, the electric rotational speed remains at 300 r/min, and the sampling period is 20 μs. As shown in Fig. 12(a), with FCS-MPC adopted, the sequence of voltage vector is $\boldsymbol{u}_0(000)$, $\boldsymbol{u}_1(100)$, $\boldsymbol{u}_0(000)$, $\boldsymbol{u}_3(010)$, $\boldsymbol{u}_7(111)$, $\boldsymbol{u}_4(011)$, and $\boldsymbol{u}_5(001)$. Meanwhile, the action periods of voltage vectors is T_{s}, or the integer multiple of T_{s}. Fig. 12(b) shows the PWM waveforms when the proposed VAP-MPC is adopted. In the figure, the sequence of voltage vector is $\boldsymbol{u}_0(000)$, $\boldsymbol{u}_5(001)$, $\boldsymbol{u}_6(101)$, $\boldsymbol{u}_7(111)$, $\boldsymbol{u}_6(101)$, $\boldsymbol{u}_7(111)$, $\boldsymbol{u}_6(101)$, $\boldsymbol{u}_5(001)$, and $\boldsymbol{u}_6(101)$. This sequence demonstrates that, when the previous optimal vector is a nonzero voltage vector, the next optimal voltage vector must be the one among itself, its adjacent two active voltage vectors, and zero voltage vector, and this agrees well with the theoretical analysis of adjacent-voltage-vector-based

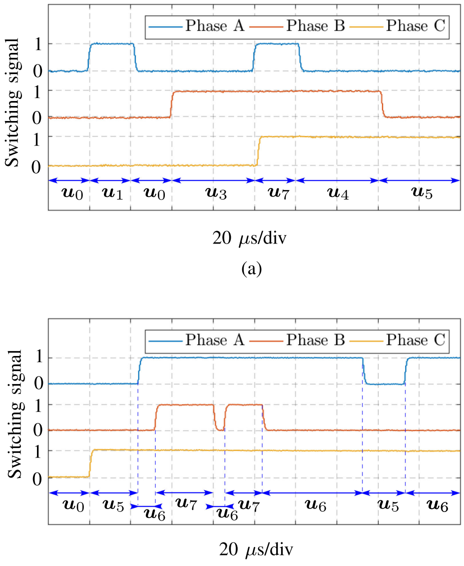

(a)

(b)

Fig. 11. Three-phase PWM waveforms (Sampling period: 20 μs). (a) Three-phase PWM waves with the FCS-MPC adopted. (b) Three-phase PWM waves with the VAP-MPC adopted.

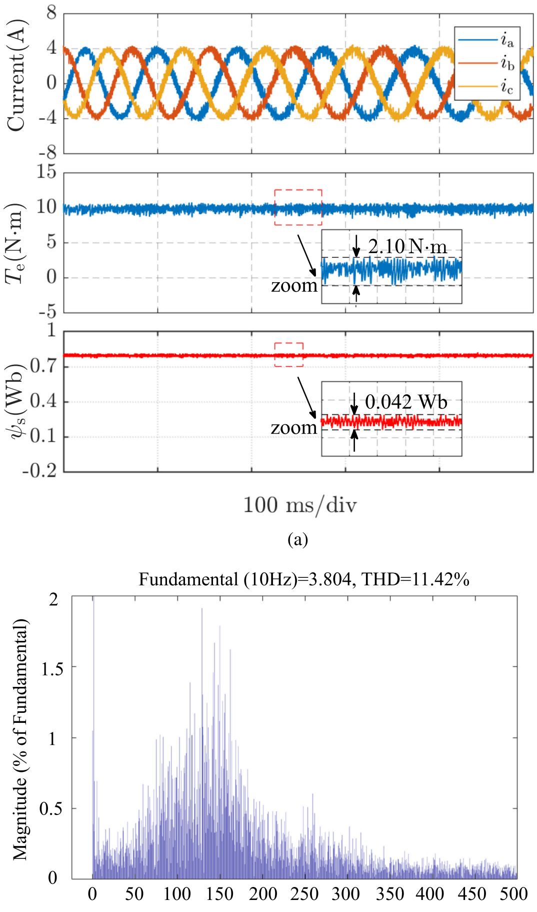

(a)

(b)

Fig. 12. Steady-state waveforms with the conventional FCS-MPC method adopted when $T_{\mathrm{e,ref}} = 10$ N·m (Average switching frequency: 2.67 kHz. Sampling period: 22 μs). (a) Waveforms of three-phase currents, electromagnetic torque T_{e}, and stator flux magnitude. (b) FFT analysis of Phase A current.

TABLE III

STEADY-STATE EXPERIMENTAL RESULTS WITH TWO METHODS ADOPTED UNDER DIFFERENT TORQUE CONDITIONS (ROTATIONAL SPEED $\omega_r = 300$ r/min)

Method	$T_{e,ref}$ (N·m)	$T_s(\mu s)$	f_{avsw}(kHz)	THD	ΔT_e (N·m)	$\psi_{s,mag}^{rms}$ (Wb)
FCS-MPC	5	22	2.64	27.47%	2.24	0.00933
VAP-MPC	5	20	2.64	21.62%	1.38	0.00684
Rate of decline				21.30%	38.39%	26.69%
FCS-MPC	7	22	2.62	19.09%	2.26	0.00973
VAP-MPC	7	20	2.61	14.85%	1.53	0.00682
Rate of decline				22.21%	32.30%	29.90%
FCS-MPC	9	22	2.65	14.05%	2.32	0.00912
VAP-MPC	9	20	2.65	11.05%	1.51	0.00672
Rate of decline				21.35%	34.91%	26.32%
FCS-MPC	11	22	2.62	11.27%	2.39	0.00901
VAP-MPC	11	20	2.64	8.26%	1.47	0.00660
Rate of decline				26.71%	38.49%	26.75%
FCS-MPC	13	22	2.61	9.46%	2.34	0.00911
VAP-MPC	13	20	2.60	6.78%	1.36	0.00650
Rate of decline				28.33%	41.88%	28.65%
FCS-MPC	15	22	2.62	7.84%	2.30	0.00874
VAP-MPC	15	19	2.61	5.37%	1.43	0.00623
Rate of decline				31.51%	37.83%	28.72%

simplified selection process. More importantly, it is proved by the PWM waveforms that the VAP could be achieved with the proposed VAP-MPC applied.

B. Steady-State Performance Comparison

In order to validate the superiority of the proposed VAP-MPC over the conventional FCS-MPC, some related steady-state comparisons were experimentally conducted. In order for a fair comparison, both methods adopt the same average switching frequency. It is calculated as

$$f_{avsw} = \frac{N_{sw}}{6} \tag{27}$$

where N_{sw} stands for the total switching times of all converter legs within a time period of 1 s.

In these steady-state tests, the torque reference is set to 10 N·m. The electric rotational speed remains at 300 r/min and the average switching frequency is around 2.65 kHz for both methods. The corresponding experimental results of three-phase currents, electromagnetic torque, and stator flux magnitude with two methods adopted are shown in Figs. 12 and 13, respectively. As shown in Fig. 12(a), the electromagnetic torque T_e fluctuates between 8.31 and 10.41 N·m. The stator flux magnitude fluctuates between 0.77 and 0.812 Wb. Meanwhile, it can be found form Fig. 12(b) that the total harmonic distortion of Phase A current is 11.42% with FCS-MPC applied. As depicted in Fig. 13(a), T_e fluctuates between 8.90 and 10.37 N·m, and the fluctuation range of the stator flux magnitude is 0.782 to 0.822 Wb. Besides, according to the FFT analysis shown in Fig. 13(b), A-phase current has relatively lower harmonic components compared with the experimental results of FCS-MPC. By comparing the results shown in Figs. 12 and 13, it is clearly visible that excellent steady-state performances can be achieved by two methods. However, when the proposed VAP-MPC is applied, the torque ripples and current harmonic components could be significantly reduced under the condition of the same average switching frequency.

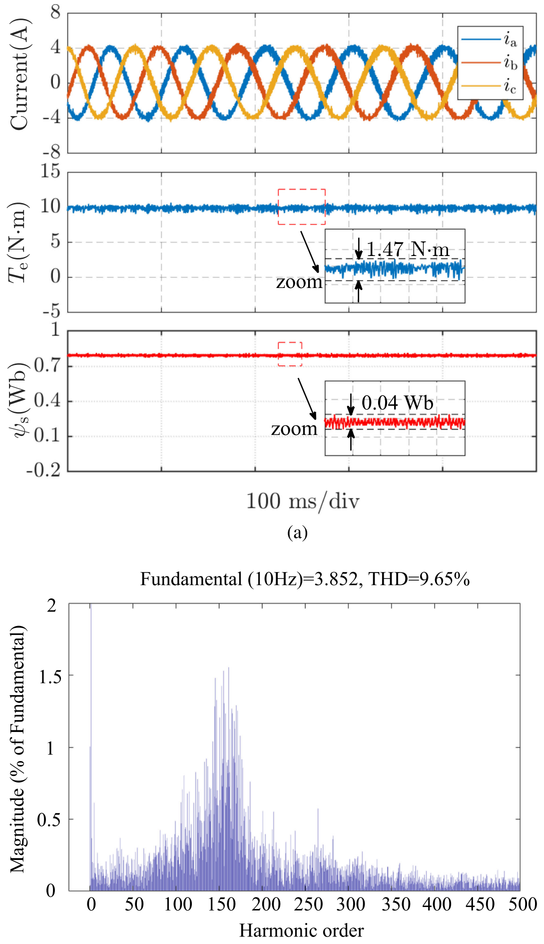

(a)

(b)

Fig. 13. Steady-state waveforms with the proposed VAP-MPC method adopted when $T_{e,ref} = 10$ N·m (Average switching frequency: 2.67 kHz. Sampling period: 20 μs). (a) Waveforms of three-phase currents, electromagnetic torque T_e, and stator flux magnitude. (b) FFT analysis of Phase A current.

In order to further analyze the superiority of the proposed method over the conventional FCS-MPC, several steady-state experiments under different torque references are carried out and the corresponding experimental results are demonstrated in Table III. It should be noted that, under the condition of the same

TABLE IV
STEADY-STATE EXPERIMENTAL RESULTS WITH TWO METHODS ADOPTED UNDER DIFFERENT ROTATIONAL SPEED (LOAD TORQUE $T_{\mathrm{L}} = 8$ N·m)

Method	ω_{r} (r/min)	$T_{\mathrm{s}}(\mu\mathrm{s})$	f_{avsw}(kHz)	THD	ΔT_{e}	$\Delta\omega_{\mathrm{r}}$ (r/min)
FCS-MPC	100	25	2.87	26.65%	4.51	13.71
VAP-MPC	100	20	2.86	21.43%	3.26	9.95
Rate of decline				19.59%	27.72%	27.43%
FCS-MPC	200	25	2.83	24.84%	4.17	15.47
VAP-MPC	200	20	2.81	18.79%	3.04	12.72
Rate of decline				24.36%	27.10%	17.78%
FCS-MPC	300	25	2.86	21.47%	4.00	20.76
VAP-MPC	300	20	2.85	16.78%	2.88	15.63
Rate of decline				21.84%	38.89%	24.71%
FCS-MPC	400	22	2.83	19.52%	3.49	18.90
VAP-MPC	400	20	2.81	14.69%	2.27	14.44
Rate of decline				24.74%	34.96%	23.60%
FCS-MPC	500	22	2.80	18.25%	3.32	18.26
VAP-MPC	500	20	2.80	14.96%	2.10	14.06
Rate of decline				18.03%	36.75%	23.00%
FCS-MPC	600	22	2.80	19.26%	3.76	20.52
VAP-MPC	600	20	2.79	14.80%	2.77	15.13
Rate of decline				23.16%	26.33%	26.27%

reference torque in these tests, the average switching frequencies for two methods are kept the same. Obviously, lower current distortions and root mean square (RMS) value of stator flux magnitude error can be expected when the proposed VAP-MPC is adopted in all different conditions, which validates the effectiveness of the proposed strategy. Besides, when the proposal is adopted, the corresponding torque ripples are reduced by 38.39%, 32.30%, 34.91%, 38.49%, 41.88%, and 37.83% when the reference torque is 5, 7, 9, 11, 13, and 15 N·m, respectively.

With the aim of further evaluating the effectiveness of the proposed VAP-MPC, the experiments were carried out under the action of the speed control loop. Similar to Table III, relative steady-state comparison experiments at different rotational speed are tested and the results are shown in Table IV. It is demonstrated that, with the same average switching frequency adopted, the corresponding torque ripples are reduced by 27.72%, 27.10%, 38.89%, 34.96%, 36.75%, and 26.33% when the rotational speed is maintained as 100, 200, 300, 400, and 500 r/min, respectively. The proposed method can effectively reduce the current distortion.

C. Dynamic Performance Comparison

Apart from steady-state performances, the transient responses of the two strategies are experimentally tested and evaluated. Figs. 15 and 14 demonstrate the experimental waveforms when the torque reference step changes from 10 to 15 N·m. The rotational speed remains 300 r/min in these tests. The average switching frequencies are both around 2.70 kHz for the two strategies. As demonstrated by these waveforms, pretty similar transient responses and excellent dynamic behaviors can be obtained by the conventional FCS-MPC and the proposed VAP-MPC, due to their inherent predictive characteristics. The electromagnetic torque can be flexibly regulated and its reference can be quickly tracked within a short period. The magnitude of the stator flux vector is kept constant at its reference value in the transient process, indicating the decoupled regulation of the torque and the stator flux.

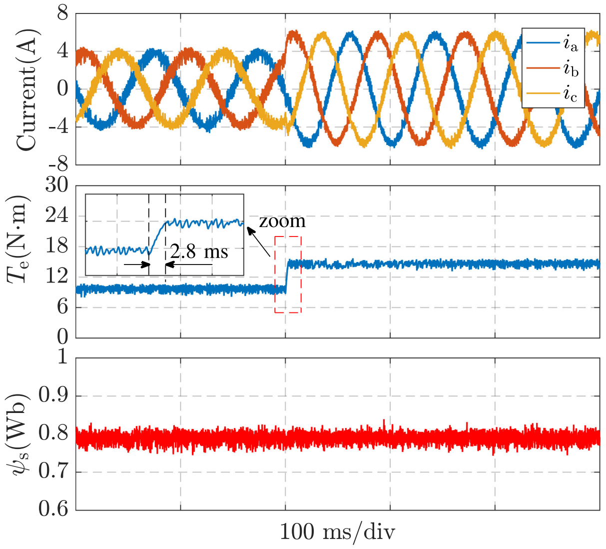

Fig. 14. Dynamic responses with proposed VAP-MPC method adopted when $T_{\mathrm{e,ref}}$ step changes from 10 to 15 N·m (Average switching frequency: 2.67 kHz. Sampling period: 20 μs). (a) Three-phase currents. (b) Electromagnetic torque T_{e}. (c) Stator flux magnitude.

In addition, Figs. 16 and 17 depict the experimental results when the reference rotational speed is step changed from 150 to 300 r/min with two method adopted, respectively. The maximum torque limit is set to 17 N·m in these tests. The average switching frequencies are kept the same for both control schemes. It is demonstrated that, with the step change of the reference speed, the torque quickly reaches its maximum limit $T_{\mathrm{e,max}}$. The rotational speed, then, increases with the maximum rising rate, and the reference speed is quickly tracked accordingly. With the rotational speed gradually rising to the reference value, the torque gradually decreases and finally stabilizes at the steady-state value. With both schemes applied, decoupled regulation of torque and flux can be expected. However, as clearly visible in these results, more significant torque ripples are generated with the conventional FCS-MPC applied.

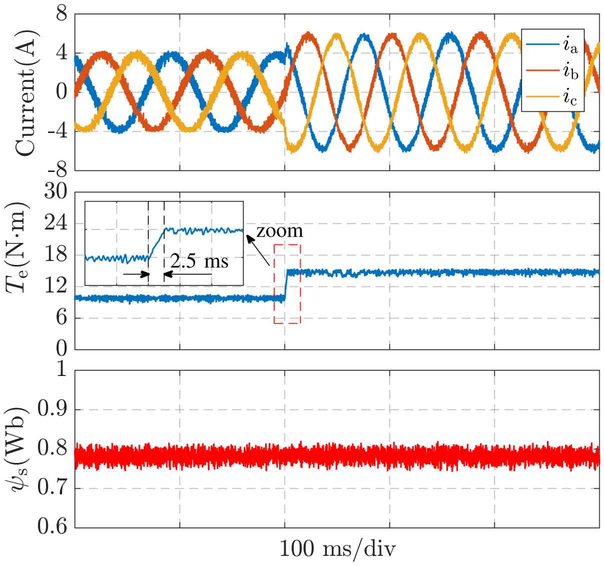

Fig. 15. Dynamic responses with conventional FCS-MPC method adopted when $T_{\mathrm{e,ref}}$ step changes from 10 to 15 N·m (Average switching frequency: 2.70 kHz. Sampling period: 22 μs). (a) Three-phase currents. (b) Electromagnetic torque T_e. (c) Stator flux magnitude.

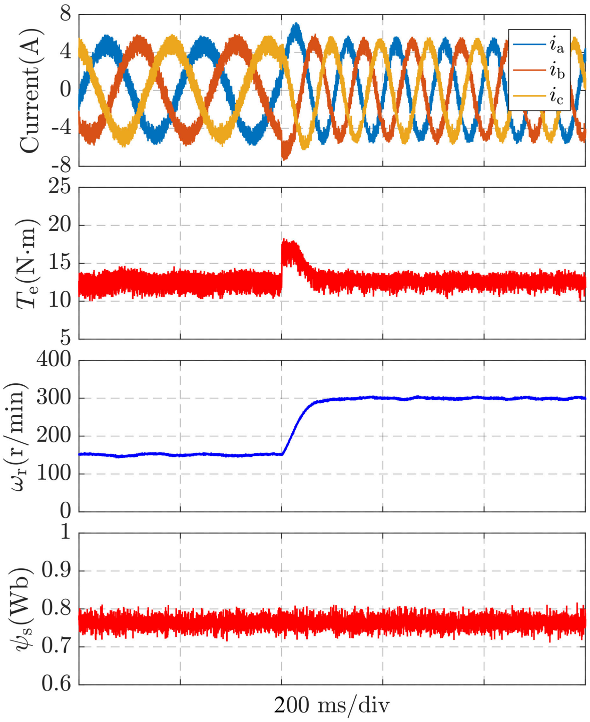

Fig. 16. Dynamic responses with conventional FCS-MPC adopted when ω_r step changes from 150 to 300 r/min (Average switching frequency: 2.82 kHz. Sampling period: 25 μs). (a) Three-phase currents. (b) Electromagnetic torque T_e. (c) Rotational speed ω_r. (d) Stator flux magnitude.

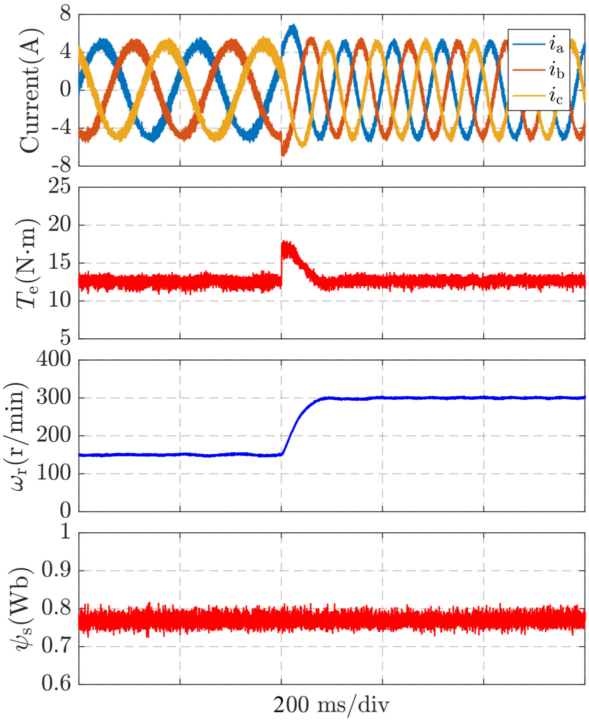

Fig. 17. Dynamic responses with proposed VAP-MPC adopted when ω_r step changes from 150 to 300 r/min (Average switching frequency: 2.85 kHz. Sampling period: 20 μs). (a) Three-phase currents. (b) Electromagnetic torque T_e. (c) Rotational speed ω_r. (d) Stator flux magnitude.

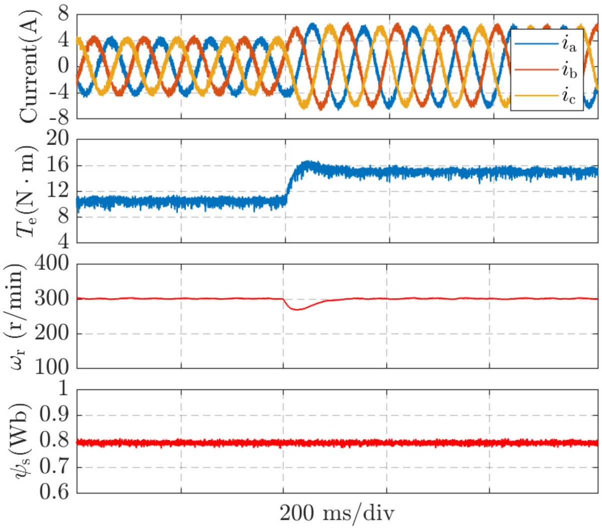

Fig. 18. Dynamic responses with the conventional FCS-MPC adopted when load torque step changes from 8 to 12 N·m (Average switching frequency: 2.90 kHz. Sampling period: 25 μs). (a) Three-phase currents. (b) Electromagnetic torque T_e. (c) Rotational speed ω_r. (d) Stator flux magnitude.

The load torque step change experiments have also been conducted to compare the dynamic behaviors of two strategies. The experimental results with load toque step change are shown in Figs. 18 and 19. In these experiments, The rotational speed remains 300 r/min and the load torque step changes from 8 to 12 N·m. The average switching frequencies are around 2.9 kHz in these experiments. It can be seen that the torque and stator flux magnitude can accurately track their reference values without overshoot or cross-coupling effects with two control strategies adopted. However, it is obvious that the three-phase current distortions and torque ripples are reduced with the proposed VAP-MPC applied.

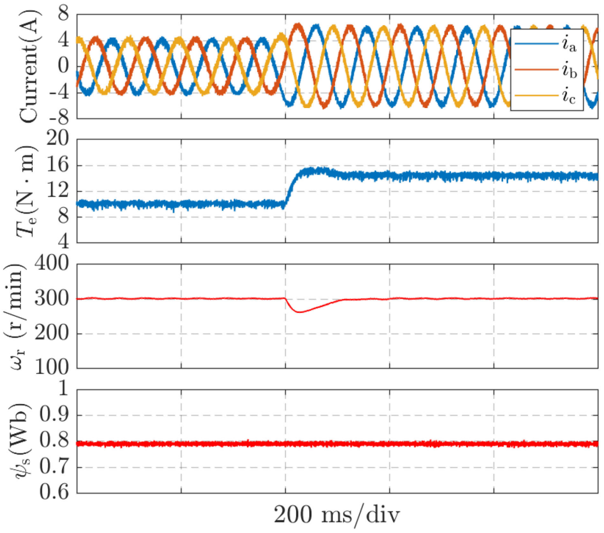

Fig. 19. Dynamic responses with the proposed VAP-MPC adopted when load torque step changes from 8 to 12 N·m (Average switching frequency: 2.9088 kHz. Sampling period: 20 μs). (a) Three-phase currents. (b) Electromagnetic torque T_e. (c) Rotational speed ω_r. (d) Stator flux magnitude.

TABLE V
COMPUTATION TIME UNDER DIFFERENT ROTATIONAL SPEED ω_r CONDITIONS

ω_r (r/min)	$t_{vap,max}$ (μs)	$t_{vap,min}$ (μs)	$t_{vap,ave}$ (μs)	$t_{fcs,ave}$ (μs)
200	14.88	9.12	12.21	12.27
300	14.56	8.48	12.07	12.26
400	14.88	9.12	11.91	12.29
500	14.72	8.32	12.01	12.24

TABLE VI
COMPUTATION TIME UNDER DIFFERENT REFERENCE TORQUE $T_{e,ref}$ CONDITIONS

$T_{e,ref}$ (N·m)	$t_{vap,max}$ (μs)	$t_{vap,min}$ (μs)	$t_{vap,ave}$ (μs)	$t_{fcs,ave}$ (μs)
7.5	13.28	7.84	10.35	10.70
10	13.25	7.04	10.38	10.73
12.5	13.28	7.81	10.24	10.71
15	13.22	7.87	10.27	10.70

D. Computational Burden Comparison

In order to compare the computational burden of the proposed VAP-MPC and the conventional FCS-MPC, additional experimental studies under different rotational speed and reference torque conditions have been conducted and the corresponding results are shown in Tables V and VI, respectively. For a fair comparison, two strategies use the same sampling frequency (i.e., 50 kHz) in the controller implementation. Additionally, when the FCS-MPC is applied, the corresponding maximum, minimum, and average computation time are almost the same. Therefore, only the average computation time of FCS-MPC method $t_{fcs,ave}$ is shown in the table.

Besides, in the proposed VAP-MPC, the expression of the VAP t_i can be obtained by means of off-line calculation based on the PMSM system model. It is applied to the implementation process to reduce the computational burden. Since a simplified selection process based on adjacent voltage vectors is adopted in the proposed VAP-MPC control strategy, the computation time will be the maximum value when the candidate voltage vector group contains eight basic voltage vectors, while it will be accordingly shortened when the candidate vector group contains itself, its adjacent two active voltage vectors, and a zero voltage vector. Furthermore, in the proposed control strategy, the action period of optimal voltage vector is variable. In the case that no switching action exists in the next sampling period (i.e., the present voltage vector will continue to act exceeding the next sampling period), the optimal voltage vector selection and its action period calculation process are not required, which reduces the computational burden significantly. In this case, the minimum computation time of VAP-MPC is obtained.

As shown in Table V, it is obvious that the average computation time of FCS-MPC and VAP-MPC varies little under different rotational speed conditions. Under the same operating condition, the maximum computation time of VAP-MPC $t_{vap,max}$ is longer than the average computation time of FCS-MPC $t_{fcs,ave}$, while the minimum value $t_{vap,min}$ is shorter than $t_{fcs,ave}$. More importantly, due to the application of the simplified voltage vector selection process, the average computation time of VAP-MPC $t_{vap,ave}$ reaches the same level as that of FCS-MPC. From the obtained results shown in Table VI, the same conclusion can be drawn.

VII. CONCLUSION

This article proposed a VAP predictive flux control strategy for PMSMs. The mathematical model of PMSM is first developed. A cost function reflecting the stator flux error is, then, constructed. Subsequently, the optimal voltage vector and its corresponding action period are determined based on a two-step cost function minimization. In addition, the digital implementation process of the proposed algorithm, including pursue problem and delay compensation, are explained in detail. Different from the conventional FCS-MPC in which the action period of selected voltage vectors is fixed to one sampling period, the proposed method can obtain improved tracking performances by regulating the action period of selected voltage vectors, as well as the selection of optimal control action. This provides an additional control freedom to reduce tracking ripples. The superiority of the proposed control scheme is validated by both experiments and comparison studies. Excellent dynamic behaviors and enhanced steady-state tracking performances can both be observed with the proposed method applied.

REFERENCES

[1] X. Zhang and Z. Li, "Sliding-mode observer-based mechanical parameter estimation for permanent magnet synchronous motor," *IEEE Trans. Power Electron.*, vol. 31, no. 8, pp. 5732–5745, Aug. 2016.

[2] X. Zhang, L. Zhang, and Y. Zhang, "Model predictive current control for PMSM drives with parameter robustness improvement," *IEEE Trans. Power Electron.*, vol. 34, no. 2, pp. 1645–1657, Feb. 2019.

[3] N. Zhao, G. Wang, D. Xu, L. Zhu, G. Zhang, and J. Huo, "Inverter power control based on DC-link voltage regulation for IPMSM drives without electrolytic capacitors," *IEEE Trans. Power Electron.*, vol. 33, no. 1, pp. 558–571, Jan. 2018.

[4] Z. Song, X. Ma, and Y. Yu, "Design of zero-sequence current controller for open-end winding PMSMs considering current measurement errors," *IEEE Trans. Power Electron.*, 2019, early access, doi: 10.1109/TPEL.2019.2952402.

[5] D. Casadei, F. Profumo, G. Serra, and A. Tani, “FOC and DTC: Two viable schemes for induction motors torque control,” *IEEE Trans. Power Electron.*, vol. 17, no. 5, pp. 779–787, Sep. 2002.

[6] T. Geyer, G. Papafotiou, and M. Morari, “Model predictive direct torque control—part I: Concept, algorithm, and analysis,” *IEEE Trans. Ind. Electron.*, vol. 56, no. 6, pp. 1894–1905, Jun. 2009.

[7] G. Papafotiou, J. Kley, K. G. Papadopoulos, P. Bohren, and M. Morari, “Model predictive direct torque control—part II: Implementation and experimental evaluation,” *IEEE Trans. Ind. Electron.*, vol. 56, no. 6, pp. 1906–1915, Jun. 2009.

[8] J. Rodriguez, R. M. Kennel, J. R. Espinoza, M. Trincado, C. A. Silva, and C. A. Rojas, “High-performance control strategies for electrical drives: An experimental assessment,” *IEEE Trans. Ind. Electron.*, vol. 59, no. 2, pp. 812–820, Feb. 2012.

[9] J. Rodriguez *et al.*, “Predictive current control of a voltage source inverter,” *IEEE Trans. Ind. Electron.*, vol. 54, no. 1, pp. 495–503, Feb. 2007.

[10] H. Aberkane, D. Sakri, and D. Rahem, “Improvement of direct torque control performances using FCS-MPC and SVM applied to PMSM: Study and comparison,” in *Proc. CISTEM*, Algiers, Algeria, Oct. 2018, pp. 1–6.

[11] T. Geyer and S. Mastellone, “Model predictive direct torque control of a five-level ANPC converter drive system,” *IEEE Trans. Ind. Appl.*, vol. 48, no. 5, pp. 1565–1575, Sep. 2012.

[12] S. Kouro, M. A. Perez, J. Rodriguez, A. M. Llor, and H. A. Young, “Model predictive control: MPC’s role in the evolution of power electronics,” *IEEE Ind. Electron. Mag.*, vol. 9, no. 4, pp. 8–21, Dec. 2015.

[13] F. Morel, X. Lin-Shi, J. Retif, B. Allard, and C. Buttay, “A comparative study of predictive current control schemes for a permanent-magnet synchronous machine drive,” *IEEE Trans. Ind. Electron.*, vol. 56, no. 7, pp. 2715–2728, Jul. 2009.

[14] Y. Zhang and H. Yang, “Model predictive torque control of induction motor drives with optimal duty cycle control,” *IEEE Trans. Power Electron.*, vol. 29, no. 12, pp. 6593–6603, Dec. 2014.

[15] H. Miranda, P. Cortes, J. I. Yuz, and J. Rodriguez, “Predictive torque control of induction machines based on state-space models,” *IEEE Trans. Ind. Electron.*, vol. 56, no. 6, pp. 1916–1924, Jun. 2009.

[16] P. Correa, M. Pacas, and J. Rodriguez, “Predictive torque control for inverter-fed induction machines,” *IEEE Trans. Ind. Electron.*, vol. 54, no. 2, pp. 1073–1079, Apr. 2007.

[17] M. Xiao, T. Shi, Y. Yan, W. Xu, and C. Xia, “Predictive torque control of permanent magnet synchronous motors using flux vector,” *IEEE Trans. Ind. Appl.*, vol. 54, no. 5, pp. 4437–4446, Sep. 2018.

[18] Z. Song, Y. Wang, and T. Shi, “A dual-loop predictive control structure for permanent magnet synchronous machines with enhanced attenuation of periodic disturbances,” *IEEE Trans. Power Electron.*, vol. 35, no. 1, pp. 760–774, Jan. 2020.

[19] J. A. Riveros, J. Prieto, F. Barrero, S. Toral, M. Jones, and E. Levi, “Predictive torque control for five-phase induction motor drives,” in *Proc. Annu. Conf. IEEE Ind. Electron. Soc.*, Nov. 2010, pp. 2467–2472.

[20] M. A. Naeem and K. M. Hasan, “Direct torque control (DTC) of three phase induction motor using model based predictive control (MPC) scheme deploying branch and bound algorithm,” in *Proc. Int. Conf. Renewable Energy Research Appl.*, Madrid, Spain, Oct. 2013, pp. 990–995.

[21] P. Cortes, M. P. Kazmierkowski, R. M. Kennel, D. E. Quevedo, and J. Rodriguez, “Predictive control in power electronics and drives,” *IEEE Trans. Ind. Electron.*, vol. 55, no. 12, pp. 4312–4324, Dec. 2008.

[22] T. Geyer, “A comparison of control and modulation schemes for medium-voltage drives: Emerging predictive control concepts versus field oriented control,” in *Proc. IEEE Energy Convers. Congr. Expo.*, Sep. 2010, pp. 2836–2843.

[23] P. Karamanakos, K. Pavlou, and S. Manias, “An enumeration-based model predictive control strategy for the cascaded h-bridge multilevel rectifier,” *IEEE Trans. Ind. Electron.*, vol. 61, no. 7, pp. 3480–3489, Jul. 2014.

[24] C. S. Lim, E. Levi, M. Jones, N. A. Rahim, and W. P. Hew, “FCS-MPC-based current control of a five-phase induction motor and its comparison with PI-PWM control,” *IEEE Trans. Ind. Electron.*, vol. 61, no. 1, pp. 149–163, Jan. 2014.

[25] Z. Song, F. Zhou, and Z. Zhang, “Parallel-observer-based predictive current control of permanent magnet synchronous machines with reduced switching frequency,” *IEEE Trans. Ind. Informat.*, 2019, early access, doi: 10.1109/TII.2019.2910842.

[26] C. Xia, T. Liu, T. Shi, and Z. Song, “A simplified finite-control-set model-predictive control for power converters,” *IEEE Trans. Ind. Informat.*, vol. 10, no. 2, pp. 991–1002, May 2014.

[27] C. Martn, M. R. Arahal, F. Barrero, M. J. Duran, and I. Gonzlez-Prieto, “Variable sampling time model predictive control of multiphase induction machines,” in *Proc. IEEE Int. Workshop Adv. Motion Control*, Mar. 2018, pp. 287–292.

[28] P. Karamanakos, P. Stolze, R. M. Kennel, S. Manias, and H. du Toit Mouton, “Variable switching point predictive torque control of induction machines,” *IEEE J. Emerg. Sel. Topics Power Electron.*, vol. 2, no. 2, pp. 285–295, Jun. 2014.

[29] N. Hoffmann, M. Andresen, F. W. Fuchs, L. Asiminoaei, and P. B. Thgersen, “Variable sampling time finite control-set model predictive current control for voltage source inverters,” in *Proc. Energy Convers. Congr. Expo.*, Sep. 2012, pp. 2215–2222.

[30] F. D. Ramirez-Figueroa and M. Pacas, “Model based control of a PMSM with variable switching frequency and torque ripple control,” in *Proc. IEEE Annu. Conf. IEEE Ind. Electron. Soc.*, Nov. 2015, pp. 001418–001423.

[31] J. Park, S. Jung, and J. Ha, “Variable time step control for six-step operation in surface-mounted permanent magnet machine drives,” *IEEE Trans. Power Electron.*, vol. 33, no. 2, pp. 1501–1513, Feb. 2018.

[32] M. R. Arahal, C. Martin, F. Barrero, I. Gonzalez-Prieto, and M. J. Duran, “Model-based control for power converters with variable sampling time: A case example using five-phase induction motor drives,” *IEEE Trans. Ind. Electron.*, vol. 66, no. 8, pp. 5800–5809, Aug. 2019.

Zhanfeng Song (M’13–SM’19) was born in Hebei, China, in 1982. He received the B.S., M.S., and Ph.D. degrees from the Tianjin University, Tianjin, China, in 2004, 2006, and 2009, respectively, all in electrical engineering.

He is currently an Associate Professor at the School of Electrical and Information Engineering, Tianjin University, China. His research interests include electrical machines and their control systems. He was the recipient of the 2018 Best Paper Award, First Prize, from IEEE Industry Applications Society Industrial Drives Committee. He served as a Guest Editor for IEEE Transactions on Industrial Informatics.

Siyu Hu was born in Henan, China, in 1995. He received the B.S. degree in electrical engineering from Chang’an University, Xi’an, China, in 2016. He is currently working toward the M.S. degree in electrical engineering with the School of Electrical and Information Engineering, Tianjin University, China.

His research interests include electrical drives and power electronics.

Bao Zhongqiang was born in Beihai City, Guangxi Province, in April 1969. He received the bachelor’s degree in engineering from Northeast Electric Power University, Jilin City, China, in July 1991.

He is currently with Guangxi Power Grid Co., Ltd., Guangxi, China. His research interest includes grid integration of new energy access systems.

Mr. Zhongqiang has won Science and Technology Progress Award of Guangxi Power Grid Co., Ltd for his research work.